Mechanics of Materials 169 (2022) 104325

Contents lists available at ScienceDirect

Mechanics of Materials

journal homepage: www.elsevier.com/locate/mechmat

Magneto-deformation and transverse elastic waves in hard-magnetic soft laminates

Quan Zhang [a], Stephan Rudykh [a,b,*]

[a] School of Mathematical and Statistical Sciences, National University of Ireland Galway, University Road, Galway, Ireland
[b] Department of Mechanical Engineering, University of Wisconsin – Madison, Madison, WI, 53706, United States

ARTICLE INFO

Keywords:
Hard-magnetic soft materials
Magnetoactive elastomers
Laminates
Finite deformations
Transverse waves
Band gaps

ABSTRACT

We study the magneto-mechanical behavior of periodic laminates made of *hard*-magnetic active elastomers (HMAEs). We formulate the amended free-energy function for HMAEs, and derive an explicit expression for the induced deformation of the HMAE laminate as a function of the applied magnetic field. Next, we employ the "small-on-large" framework and examine the small-amplitude shear waves propagating in the finitely deformed HMAE laminate in a magnetic field.

We find that the remanent magnetization of HMAE phases can result in compressive deformations (in the direction of the applied magnetic field), as opposed to the induced tensile deformation in previously considered *soft*-magnetic active laminates. Further, we derive the dispersion relations for the transverse elastic waves propagating in the direction perpendicular to the layers. We use the analytical results to illustrate the tunability of the shear wave band gaps with varying remanent magnetizations of the phases; moreover, the shear wave band gaps can be actively controlled by a remotely applied magnetic field.

1. Introduction

Magnetoactive elastomers (MAEs) are composite materials consisting of magnetizable particles embedded in a soft matrix. Under an externally applied magnetic field, the magnetized particles interact, resulting in modification of the mechanical properties and leading to deformation occurring mostly in the matrix. The remote and reversible principle of actuation and property tunability makes the materials attractive for the development of variable-stiffness devices (Erb et al., 2012; Ginder et al., 2002), vibration absorbers (Ginder et al., 2001; Li et al., 2014) and isolators (Opie and Yim, 2011), actuators (Kashima et al., 2012; Tang et al., 2018), and sensors (Tian et al., 2011), and biomedical devices (Makarova et al., 2016) among others. Typically, a polymeric matrix material (e.g., silicone rubber) in its liquid state before polymerization, is mixed with magnetizable particles of micro or even nano size. Curing in the presence of magnetic field results in the formation of chainlike structures aligned along the direction of the magnetic field. Through this microstructure modification, different interactions between magnetizable particles are induced, thus, enabling tunability of the overall magneto-mechanical behavior of MAEs.

The foundation of magneto-elasticity (and mathematically analogous electro-elasticity) was developed by Truesdell and Toupin (1960). Since then, the magneto-elastic theory has been further developed by Dorfmann and Ogden (2003, 2004), Bustamante et al. (2006), Vu and Steinmann (2007), and Destrade and Ogden (2011). In parallel, significant efforts have been made towards the development and implementation of nonlinear magneto-elasticity into numerical schemes (Haldar et al., 2016; Labusch et al., 2014; Metsch et al., 2016). An analytical approach for estimating the response and effective properties of MAEs with the random distribution of magnetoactive particles has been developed by Ponte Castañeda and Galipeau (2011). Galipeau et al. (2014) showed that MAEs with seemingly similar microstructures might exhibit significantly different magneto-mechanical properties. Rudykh and Bertoldi (2013) employed a micromechanics approach to analyze the macroscopic stability in anisotropic MAEs. Goshkoderia and Rudykh (2017) have investigated the long-wave instability in particulate MAE composites via a numerical homogenization. Goshkoderia et al. (2020) have reported the experimental observations of the instability-induced patterns in soft magneto-sensitive periodic systems. More recently, Pathak et al. (2022) studied the onset of microscopic instabilities in MAEs with bi-phasic layered microstructure exhibiting ferromagnetic behavior.

* Corresponding author. School of Mathematical and Statistical Sciences, National University of Ireland Galway, University Road, Galway, Ireland.
E-mail address: rudykh@wisc.edu (S. Rudykh).

https://doi.org/10.1016/j.mechmat.2022.104325
Received 16 March 2022; Accepted 11 April 2022
Available online 18 April 2022

The aforementioned MAEs belong to so-called *soft*-magnetic active elastomers, typically based on embedding particles such as iron, soft ferrite, iron-silicon alloys, iron-nickel alloys (Jolly et al., 1996). These soft-magnetic materials have low coercivity and do not retain remanent magnetization once the external magnetic field has been removed (Bertotti, 1998). Recently, particles of high-coercivity ferromagnetic materials or hard-magnetic materials (such as NdFeB, hard ferrite, alnico alloys, samarium-cobalt) have been used to fabricate *hard*-magnetic active elastomers (HMAEs). These new magnetoactive composites showed programmable and complex shape transformations at *low* magnetic fields (Kim et al., 2018; Lum et al., 2016; Montgomery et al., 2020; Yan et al., 2021b). Once exposed to a large magnetic field, hard-magnetic materials retain their magnetization even after removing the external field. The high coercivity allows the hard-magnetic materials to sustain their remanent magnetization over a wide range of applied magnetic fields (that are below the coercive field strength). When the applied magnetic field is not aligned with the magnetization direction of the hard-magnetic particles, the induced magnetic torque acts to align the particle's magnetization direction with the applied field, leading to deformation of the HMAE composite. The remote and reversible shape-transformative behavior of HMAEs has enabled functionalities in areas such as soft robotics (Cui et al., 2019; Hu et al., 2018), biomedicine (Wang et al., 2021), mechanical metamaterials (Chen et al., 2021), self-assembly and self-organization (Piranda et al., 2021), and actuation (Bowen et al., 2015; Crivaro et al., 2016). To describe the behavior of the materials, Zhao et al. (2019) proposed a phenomenological model for ideal HMAEs. In the model, the magnetic flux density in the material is assumed to be linear with the external field strength, with the permeability constant equal to that of the vacuum. Yan et al. (2021a) have extended the model to both uniform and non-uniform magnetic fields. Garcia-Gonzalez and Hossain (2021) have proposed a lattice-based model that incorporates information of the particles' distribution into the constitutive formulations. A recent review by Lucarini et al. (2022) summarizes the development in the field of HMAEs.

The material tunability by a remotely magnetic field – either through property modification or induced deformation – holds the intriguing potential for designing metamaterials for elastic wave manipulation. The foundation of the analysis of infinitesimal motion superimposed on finite deformations can be found in the work of Green et al. (1952), further developed by Ogden (2007), and is widely adopted as "small--on-large" theory (Bertoldi and Boyce, 2008; Guo et al., 2017, 2022; Norris and Parnell, 2012; Rudykh and Boyce, 2014). Here, we employ the small-on-large framework to examine the propagation of small-amplitude elastic waves in finitely deformed magnetoelastic materials. Following the work by Maugin (1981), providing the governing equations for magnetoelastic waves in magnetizable deformable materials, the nonlinear surface waves (Abd-Alla and Maugin, 1987; Hefni et al., 1995) and inhomogeneous plane waves (Boulanger, 1989) have been studied. Based on the formulation of Dorfmann and Ogden (2004), Destrade and Ogden (2011) examined the small-amplitude plane harmonic waves in the finitely strained magnetoelastic material. Saxena and Ogden (2011, 2012) studied the Rayleigh surface and Love waves propagating in a finitely strained isotropic and layered half-space magnetoelastic solid immersed in a magnetic field. Recently, Karami Mohammadi et al. (2019) have investigated transverse elastic wave propagation in finitely deformed bi-phase periodic magnetoelastic layered composites, and illustrated the shear wave bandgap tunability by magnetically induced deformation. However, these aforementioned works considered soft-magnetic active elastomers, while little is known about the wave propagation in HMAE medium.

In this work, we investigate the finite deformation and superimposed small-amplitude transverse elastic waves in bi-phasic layered HMAEs with remanent magnetization. We study the magnetostriction of the periodic layered HMAEs and derive the expression for the induced deformation as a function of the applied magnetic field, mechanical and magnetic properties of the phases, and their volume fractions. Moreover, we analyze the influences of the applied magnetic field and material parameters – especially the remanent magnetization – on the shear wave band gaps in the HMAE laminates.

2. Theoretical background

2.1. Nonlinear magneto-elasticity

Consider a magnetoelastic deformable solid occupying domain Ω_0 in the reference configuration where no magnetic and mechanical fields are applied. Under the action of combined magnetic and mechanical loadings, the magnetoelastic solid occupies a deformed configuration denoted as Ω. The deformation is described by a function $\mathbf{x} = \mathbf{x}(\mathbf{X})$ that maps the material point $\mathbf{X}$ from the reference state to the new position $\mathbf{x}$ in the deformed state. The deformation gradient is thus defined as $\mathbf{F} = \partial\mathbf{x}/\partial\mathbf{X}$. For incompressible solids, $J \equiv \det\mathbf{F} = 1$.

Here, we follow the work by Dorfmann and Ogden (2004) and denote by $\mathbf{B}$, $\mathbf{H}$, and $\mathbf{M}$, respectively, the magnetic induction, the magnetic field, and the magnetization in the deformed configuration. They are related as

$$\mathbf{B} = \mu_0(\mathbf{H} + \mathbf{M}), \tag{1}$$

where the constant μ_0 is the magnetic permeability in a vacuum. Neglecting electrical, thermal, and relativistic effects, the quasi-static Maxwell equations in terms of the magnetic induction $\mathbf{B}$ and the magnetic field $\mathbf{H}$ in the deformed state, can be written as

$$\mathrm{div}\mathbf{B} = 0 \quad \text{and} \quad \mathrm{curl}\mathbf{H} = \mathbf{0}. \tag{2}$$

Here and thereafter, the upper case first letter denotes the differential operator in the reference configuration, whereas the lower case denotes the ones in the deformed configuration. The magnetostatic equations in the reference configuration are

$$\mathrm{Div}\mathbf{B}_L = 0 \quad \text{and} \quad \mathrm{Curl}\mathbf{H}_L = \mathbf{0}, \tag{3}$$

where $\mathbf{B}_L = \mathbf{F}^{-1}\cdot\mathbf{B}$ and $\mathbf{H}_L = \mathbf{F}^T\cdot\mathbf{H}$ are the Lagrangian counterparts of the magnetic induction and the magnetic field, respectively.

Following the work of Kovetz (2000), the magnetization is defined in terms of the specific free-energy density φ ($\mathbf{F}$, $\mathbf{B}$) as

$$\mathbf{M} = -\rho\frac{\partial\varphi(\mathbf{F},\mathbf{B})}{\partial\mathbf{B}}, \tag{4}$$

where ρ is the density in the deformed configuration. The *total* Cauchy stress $\boldsymbol{\sigma}$ can then be written in the form

$$\boldsymbol{\sigma} = \rho\frac{\partial\varphi(\mathbf{F},\mathbf{B})}{\partial\mathbf{F}}\mathbf{F}^T + (\mathbf{M}\cdot\mathbf{B})\mathbf{I} - \mathbf{M}\otimes\mathbf{B} + \mathbf{T}^M, \tag{5}$$

where

$$\mathbf{T}^M = \frac{1}{\mu_0}\mathbf{B}\otimes\mathbf{B} - \frac{1}{2\mu_0}(\mathbf{B}\cdot\mathbf{B})\mathbf{I} \tag{6}$$

is the so-called Maxwell stress. The specific free-energy density in the Lagrangian form is defined as $\Phi(\mathbf{F},\mathbf{B}_L) = \varphi(\mathbf{F},\mathbf{F}\mathbf{B}_L)$. In terms of Φ, an "amended" free-energy function has been proposed by Dorfmann and Ogden (2004)

$$W(\mathbf{F},\mathbf{B}_L) = \rho_0\Phi(\mathbf{F},\mathbf{B}_L) + \frac{\mathbf{F}\mathbf{B}_L\cdot\mathbf{F}\mathbf{B}_L}{2\mu_0}, \tag{7}$$

where $\rho_0 = \rho$ (J = 1) is the density in the reference configuration. Thus, the total first Piola-Kirchhoff stress tensor $\mathbf{P}$, and Lagrangian magnetic field $\mathbf{H}_L$ are

$$\mathbf{P} = \frac{\partial W(\mathbf{F},\mathbf{B}_L)}{\partial\mathbf{F}} - p\mathbf{F}^{-T} \quad \text{and} \quad \mathbf{H}_L = \frac{\partial W(\mathbf{F},\mathbf{B}_L)}{\partial\mathbf{B}_L}. \tag{8}$$

Here, p is the Lagrange multiplier introduced due to the incompressibility constraint. Correspondingly, the total Cauchy stress tensor is

$$\boldsymbol{\sigma} = \frac{\partial W(\mathbf{F}, \mathbf{B}_L)}{\partial \mathbf{F}} \mathbf{F}^T - p\mathbf{I}. \tag{9}$$

Under the quasi-static condition and in the absence of body forces, the total Cauchy and first Piola-Kirchhoff stresses satisfy the following equilibrium equations

$$\mathrm{div}\boldsymbol{\sigma} = \mathbf{0} \quad \text{and } \mathrm{Div}\mathbf{P} = \mathbf{0}. \tag{10}$$

2.2. Incremental motions

Next, we consider an infinitesimal incremental motion superimposed on the deformed state. We denote the incremental changes in $\mathbf{F}$, p, $\mathbf{P}$, $\mathbf{B}_L$, and $\mathbf{H}_L$ as $\dot{\mathbf{F}}$, $\dot{p}$, $\dot{\mathbf{P}}$, $\dot{\mathbf{B}}_L$, and $\dot{\mathbf{H}}_L$, respectively. According to Eq. (8), the linearized constitutive relations can be written as

$$\begin{aligned} \dot{\mathbf{P}} &= \mathbb{C}_0 : \dot{\mathbf{F}} + \mathscr{B}_0 \cdot \dot{\mathbf{B}}_L - \dot{p}\mathbf{F}^{-T} + p\mathbf{F}^{-T} \cdot \dot{\mathbf{F}}^T \cdot \mathbf{F}^{-T} \\ \dot{\mathbf{H}}_L &= \dot{\mathbf{F}} : \mathscr{B}_0 + \mathbf{K}_0 \cdot \dot{\mathbf{B}}_L \end{aligned} \tag{11}$$

where

$$\mathbb{C}_0 = \frac{\partial^2 W}{\partial \mathbf{F} \partial \mathbf{F}}, \quad \mathscr{B}_0 = \frac{\partial^2 W}{\partial \mathbf{F} \partial \mathbf{B}_L}, \quad \mathbf{K}_0 = \frac{\partial^2 W}{\partial \mathbf{B}_L \partial \mathbf{B}_L}. \tag{12}$$

The "push-forward" counterparts (in the deformed configuration) of the incremental changes $\dot{\mathbf{P}}$, $\dot{\mathbf{B}}_L$, and $\dot{\mathbf{H}}_L$ are

$$\dot{\boldsymbol{\sigma}} = \dot{\mathbf{P}} \cdot \mathbf{F}^T, \ \dot{\mathbf{B}} = \mathbf{F} \cdot \dot{\mathbf{B}}_L, \quad \text{and} \quad \dot{\mathbf{H}} = \mathbf{F}^{-T} \cdot \dot{\mathbf{H}}_L. \tag{13}$$

Denoting $\mathbf{u} = \dot{\mathbf{x}}$ as the infinitesimal incremental displacement superimposed on the deformed state, the incremental constitutive laws in Eq. (11) becomes

$$\begin{aligned} \dot{\boldsymbol{\sigma}} &= \mathbb{C} : \mathbf{U} + \mathscr{B} \cdot \dot{\mathbf{B}} - \dot{p}\mathbf{I} + p\mathbf{U}^T \\ \dot{\mathbf{H}} &= \mathbf{U} : \mathscr{B} + \mathbf{K} \cdot \dot{\mathbf{B}} \end{aligned} \tag{14}$$

where $\mathbf{U} = \mathrm{grad}\mathbf{u} = \dot{\mathbf{F}} \cdot \mathbf{F}^{-1}$. The incompressibility constraint yields

$$\mathrm{tr}\mathbf{U} = \mathrm{div}\mathbf{u} = 0. \tag{15}$$

The updated tensors of the magnetoelastic moduli in Eq. (14) are

$$\begin{aligned} \mathbb{C}_{ijkl} &= \mathbb{C}_{0irks} F_{jr} F_{ls} \\ \mathscr{B}_{ijk} &= \mathscr{B}_{0irm} F_{jr} F^{-1}_{mk} \\ \mathbf{K} &= \mathbf{F}^{-T} \cdot \mathbf{K}_0 \cdot \mathbf{F}^{-1} \end{aligned} \tag{16}$$

The corresponding incremental equations of motion are

$$\mathrm{div}\dot{\boldsymbol{\sigma}} = \rho \mathbf{u}_{,tt}, \ \mathrm{div}\dot{\mathbf{B}} = 0, \quad \text{and } \mathrm{curl}\dot{\mathbf{H}} = \mathbf{0}. \tag{17}$$

We consider steady-state small amplitude waves propagating in the deformed magnetoelastic medium. Following Destrade and Ogden (2011), the solution for Eq. (17) can be written in the form of plane waves with constant polarization

$$\begin{aligned} \mathbf{u} &= \mathbf{g}\, f(\mathbf{n} \cdot \mathbf{x} - ct) \\ \dot{\mathbf{B}} &= \mathbf{d}\, q(\mathbf{n} \cdot \mathbf{x} - ct) \\ \dot{p} &= \Pi(\mathbf{n} \cdot \mathbf{x} - ct) \end{aligned} \tag{18}$$

where $\mathbf{g}$ and $\mathbf{d}$ are constant unit vectors denoting polarizations, f, q, and Π are single-variable functions with respect to the argument $\mathbf{n} \cdot \mathbf{x} - ct$, and $\mathbf{n}$ is the constant unit vector denoting the direction of propagation. The use of the incompressibility constraint in Eq. (15) and the incremental motion of Eq. $(17)_2$ yields

$$\mathbf{g} \cdot \mathbf{n} = 0 \quad \text{and} \quad \mathbf{d} \cdot \mathbf{n} = 0. \tag{19}$$

3. Results and examples

3.1. Energy density function for HMAEs

Due to the relatively large coercivity, hard-magnetic materials can retain high remanent magnetization even in the absence of an externally applied magnetic field once they are saturated. The high coercivity further allows the magnetic materials to sustain the remanent magnetization over a wide range of applied magnetic fields (below the coercivity level). The magnetic behavior of the HMAEs can be approximated by a linear function when the applied magnetic field is below the coercivity level (Zhao et al., 2019).

As illustrated in Fig. 1a, we assume that the magnetic induction $\mathbf{B}$ of the HMAEs is linearly related to the applied magnetic field $\mathbf{H}$ when the field strength is small enough relative to the coercivity level (Lovatt and Watterson, 1999), namely

$$\mathbf{B} = \mathbf{B}_r + \mu \mathbf{H}, \tag{20}$$

where $\mathbf{B}_r$ is the remanent induction and is related to the remanent magnetization $\mathbf{M}_r$ by $\mathbf{B}_r = \mu_0 \mathbf{M}_r$. The combination of Eqs. (1) and (20) yields

$$\mathbf{M} = (\mu_r - 1)\mathbf{H} + \mathbf{M}_r, \tag{21}$$

where $\mu_r = \mu/\mu_0$ is the relative magnetic permeability. The idealized magnetization loop with the linear region represented by Eq. (21) is illustrated in Fig. 1b. Alternatively, the magnetization can be expressed with respect to the magnetic induction

$$\mathbf{M} = \frac{\mathbf{B}}{\mu_0} \chi + \frac{1}{\mu_r} \mathbf{M}_r, \tag{22}$$

where $\chi = (\mu - \mu_0)/\mu$ is the magnetic susceptibility. Based on Eq. (22), the specific free-energy function can be written as

$$\rho\varphi(\mathbf{F}, \mathbf{B}) = w_e - \frac{1}{2\mu_0} \mathbf{B} \cdot \chi \mathbf{B} - \frac{1}{\mu_r} \mathbf{B} \cdot \mathbf{M}_r, \tag{23}$$

where w_e denotes the purely elastic response of the HMAEs. The constructed specific free-energy function satisfies Eq. (4). Therefore, the Lagrangian form of the specific free-energy function is

$$\rho_0 \Phi(\mathbf{F}, \mathbf{B}_L) = W_e(\mathbf{F}) - \frac{1}{2\mu_0} \mathbf{F}\mathbf{B}_L \cdot \chi \mathbf{F}\mathbf{B}_L - \frac{1}{\mu_r} \mathbf{F}\mathbf{B}_L \cdot \mathbf{R}\mathbf{M}_{Lr}, \tag{24}$$

where $W_e(\mathbf{F})$ can be defined by the appropriate hyperelastic energy potentials. In Eq. (24), $\mathbf{M}_{Lr}$ is the remanent magnetization in the Lagrangian description. It is related to the remanent magnetization in the deformed configuration via $\mathbf{R}\mathbf{M}_{Lr} = \mathbf{M}_r$, where $\mathbf{R}$ is the rotational component of the deformation gradient $\mathbf{F}$. Such a definition is adopted since the remanent magnetization $\mathbf{M}_r$ in the deformed configuration is determined by the rotations of the HMAEs, independently of stretches. This relation has been examined by Mukherjee et al. (2021) through full-field homogenization simulations, showing some similarities with the behavior of the isotropic soft-magnetic MAEs (Danas et al., 2012). Recalling Eq. (7), the Lagrangian amended energy function can be written as

$$W(\mathbf{F}, \mathbf{B}_L) = W_e(\mathbf{F}) + \frac{1}{2\mu} \mathbf{F}\mathbf{B}_L \cdot \mathbf{F}\mathbf{B}_L - \frac{1}{\mu_r} \mathbf{F}\mathbf{B}_L \cdot \mathbf{R}\mathbf{M}_{Lr}. \tag{25}$$

Upon substitution of Eq. (25) into Eq. (9), the total Cauchy stress in the HMAEs is evaluated as

$$\boldsymbol{\sigma} = \mathbf{P}\mathbf{F}^T = \frac{\partial W_e(\mathbf{F})}{\partial \mathbf{F}} \mathbf{F}^T - p\mathbf{I} + \frac{1}{\mu} \mathbf{B} \otimes \mathbf{B} - \frac{1}{\mu_r} \mathbf{M}_r \otimes \mathbf{B}. \tag{26}$$

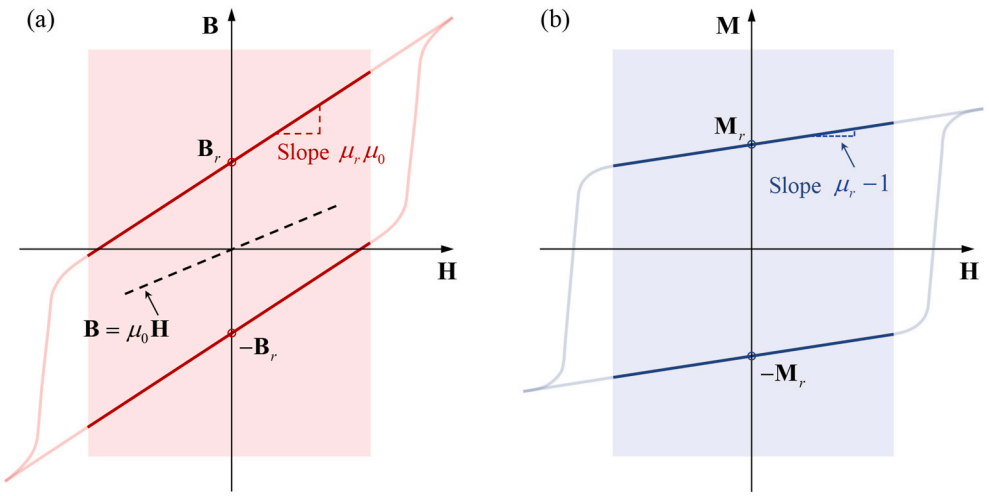

Fig. 1. The illustration of typical magnetic hysteresis behavior of HAMEs in terms of (a) the B–H curve and (b) the M − H curve. Here, a linear hard-magnetic behavior is assumed for the applied magnetic field far below the coercivity. The slopes of the linear regions on the B–H and M−H curves are $\mu_r\mu_0$ and μ_r-1, respectively, where μ_0 is the permeability of vacuum and μ_r is the relative magnetic permeability.

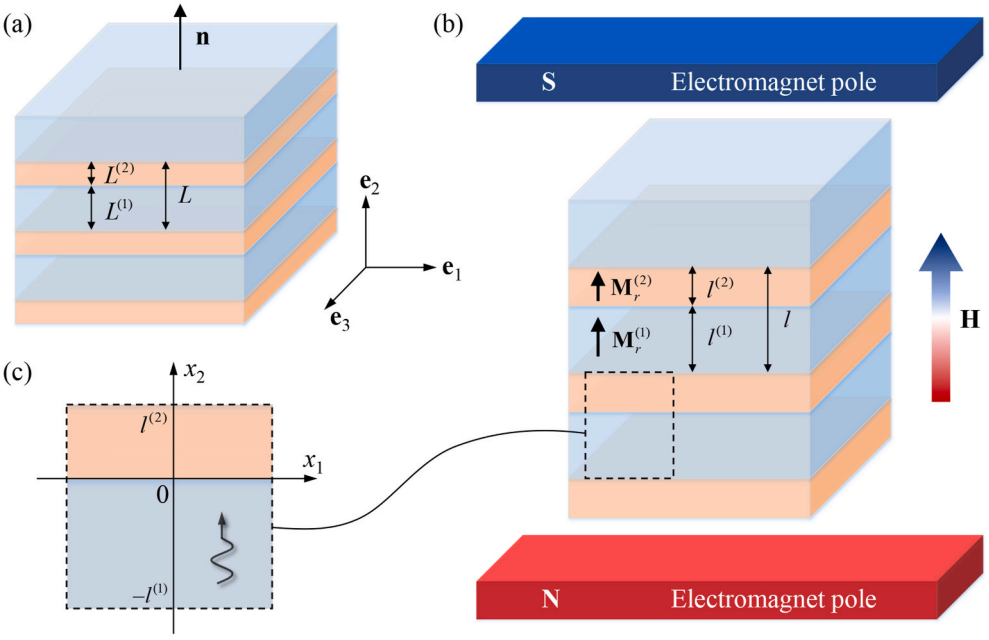

Fig. 2. HMAE laminates with bi-phasic layered microstructure in (a) the reference (undeformed) state, and (b) the magnetic field induced deformed state; (c) a representative unit cell.

3.2. HMAE laminates

Consider periodic laminates consisting of two isotropic incompressible alternating HMAE phases with volume fractions $v^{(1)}$ and $v^{(2)}=1-v^{(1)}$. Denoting the periodic constant of the undeformed laminate as L, the alternating layer thicknesses will be $L^{(1)}=v^{(1)}L$ and $L^{(2)}=v^{(2)}L$, respectively (see Fig. 2a).

We consider the case when the remanent magnetizations in the laminates are in the same direction as the applied field (in the $\mathbf{e}_2$ direction; see Fig. 2b), namely

$$\mathbf{M}_r^{(1)}=M_r^{(1)}\mathbf{e}_2 \quad \text{and} \quad \mathbf{M}_r^{(2)}=M_r^{(2)}\mathbf{e}_2. \tag{27}$$

Under the action of the applied field, the laminate stretches along the $\mathbf{e}_2$ direction. In the deformed laminate, the layer thicknesses become

$$l^{(1)}=\lambda_2^{(1)}L^{(1)}, \quad l^{(2)}=\lambda_2^{(2)}L^{(2)}, \quad \text{and} \quad l=\overline{\lambda}_2 L, \tag{28}$$

where $\lambda_2^{(1)}$ and $\lambda_2^{(2)}$ are the phase stretch ratios in the $\mathbf{e}_2$ direction and $\overline{\lambda}_2=v^{(1)}\lambda_2^{(1)}+v^{(2)}\lambda_2^{(2)}$. Here and thereafter, the parameters of the alternating layers are denoted as $(\bullet)^{(1)}$ and $(\bullet)^{(2)}$, respectively.

The average deformation gradient and Eulerian magnetic induction are defined as

$$\overline{\mathbf{F}}=v^{(1)}\mathbf{F}^{(1)}+v^{(2)}\mathbf{F}^{(2)}=\lambda\mathbf{e}_2\otimes\mathbf{e}_2+\lambda^{-1/2}(\mathbf{I}-\mathbf{e}_2\otimes\mathbf{e}_2) \tag{29}$$

and

$$\overline{\mathbf{B}}=v^{(1)}\mathbf{B}^{(1)}+v^{(2)}\mathbf{B}^{(2)}=B\mathbf{e}_2, \tag{30}$$

respectively. The displacement continuity condition along the interface between the layers enforces

$$\left(\mathbf{F}^{(1)}-\mathbf{F}^{(2)}\right)\cdot\mathbf{s}=\mathbf{0}, \tag{31}$$

where $\mathbf{s}$ is an arbitrary unit vector perpendicular to $\mathbf{n}$ (the unit vector denoting the lamination direction; see Fig. 2a). Using Eq. (31) and the symmetry of the deformation gradient defined in Eq. (29) with the phase incompressibility, we obtain $\lambda_2^{(1)}=\lambda_2^{(2)}=\lambda$. Therefore, the deformation gradients in alternating phases are

$$\mathbf{F}^{(1)}=\mathbf{F}^{(2)}=\lambda\mathbf{e}_2\otimes\mathbf{e}_2+\lambda^{-1/2}(\mathbf{I}-\mathbf{e}_2\otimes\mathbf{e}_2). \tag{32}$$

The traction continuity condition across the interface between the layers implies that

$$\left(\boldsymbol{\sigma}^{(1)}-\boldsymbol{\sigma}^{(2)}\right)\cdot\mathbf{n}=\mathbf{0}. \tag{33}$$

Moreover, in the absence of free current at the interface, the jump conditions for the Eulerian magnetic induction and magnetic field are

$$\left(\mathbf{B}^{(1)}-\mathbf{B}^{(2)}\right)\cdot\mathbf{n}=0 \quad \text{and} \quad \left(\mathbf{H}^{(1)}-\mathbf{H}^{(2)}\right)\times\mathbf{n}=\mathbf{0}. \tag{34}$$

Using the magnetic induction jump condition $(34)_1$, for the macroscopically applied magnetic load defined in Eq. (30), we obtain

$$\mathbf{B}^{(1)}=\mathbf{B}^{(2)}=B\mathbf{e}_2. \tag{35}$$

3.3. Magneto-deformation

Consider the laminates consisting of HMAE phases, whose constitutive behavior is governed by the energy function (25); we assume that their purely elastic response is expressed as a function of the first invariant of the right Cauchy-Green deformation tensor $\mathbf{C}^{(\xi)}=(\mathbf{F}^{(\xi)})^T\cdot\mathbf{F}^{(\xi)}$, namely

$$W_e^{(\xi)}\left(\mathbf{F}^{(\xi)}\right)=\Psi_e^{(\xi)}\left(I_1^{(\xi)}\right), \tag{36}$$

where $I_1^{(\xi)}=\mathbf{F}^{(\xi)}:\mathbf{F}^{(\xi)}$. Thus, the stress field in the layer ξ ($\xi=1,2$) is

$$\boldsymbol{\sigma}^{(\xi)}=2\Psi_1^{(\xi)}\mathbf{F}^{(\xi)}\cdot\left(\mathbf{F}^{(\xi)}\right)^T-p^{(\xi)}\mathbf{I}+\frac{1}{\mu^{(\xi)}}\mathbf{B}^{(\xi)}\otimes\mathbf{B}^{(\xi)}-\frac{1}{\mu_r^{(\xi)}}\mathbf{M}_r^{(\xi)}\otimes\mathbf{B}^{(\xi)}, \tag{37}$$

where $\Psi_1^{(\xi)}=\partial\Psi_e^{(\xi)}/\partial I_1^{(\xi)}$. The nonzero stress components are

$$\begin{aligned}&\sigma_{11}^{(\xi)}=\sigma_{33}^{(\xi)}=2\Psi_1^{(\xi)}\lambda^{-1}-p^{(\xi)} \quad \text{and}\\ &\sigma_{22}^{(\xi)}=2\Psi_1^{(\xi)}\lambda^2-p^{(\xi)}+\frac{B^2}{\mu^{(\xi)}}-\frac{1}{\mu_r^{(\xi)}}M_r^{(\xi)}B\end{aligned} \tag{38}$$

We assume that the HMAE laminate is surrounded by a vacuum, and no mechanical loadings are applied. The stress field jump condition across the interface between the laminate and vacuum yields

$$v^{(1)}\boldsymbol{\sigma}^{(1)}+v^{(2)}\boldsymbol{\sigma}^{(2)}=\boldsymbol{\sigma}_m^*, \tag{39}$$

where

$$\boldsymbol{\sigma}_m^*=\frac{1}{\mu_0}\left(\mathbf{B}^*\otimes\mathbf{B}^*-\frac{1}{2}(\mathbf{B}^*\cdot\mathbf{B}^*)\mathbf{I}\right) \tag{40}$$

is the Maxwell stress in the vacuum. Once again, the magnetic induction jump condition across the interface between the laminate and vacuum enforces $\mathbf{B}^*=\overline{\mathbf{B}}=B\mathbf{e}_2$.

For simplicity, we consider that the purely elastic response of the HMAE phases is dictated by the neo-Hookean model, namely

$$\Psi_e^{(\xi)}\left(I_1^{(\xi)}\right)=\frac{G^{(\xi)}}{2}\left(I_1^{(\xi)}-3\right), \tag{41}$$

Where $G^{(\xi)}$ is the shear modulus. Using Eqs. (33) and (38)-(41), we obtain

$$\begin{aligned}&\overline{G}\lambda^{-1}-\left(v^{(1)}p^{(1)}+v^{(2)}p^{(2)}\right)=-\frac{B^2}{2\mu_0} \quad \text{and}\\ &G^{(\xi)}\lambda^2-p^{(\xi)}+\frac{B^2}{\mu^{(\xi)}}-\frac{1}{\mu_r^{(\xi)}}M_r^{(\xi)}B=\frac{B^2}{2\mu_0}\end{aligned} \tag{42}$$

where $\overline{G}=v^{(1)}G^{(1)}+v^{(2)}G^{(2)}$. By eliminating the Lagrange multipliers from Eq. (42), we obtain the expression of the induced deformation as a function of the magnetic induction, mechanical and magnetic properties of layers, and their volume fractions, namely

$$\lambda^2-\frac{1}{\lambda}=\frac{B^2}{\overline{G}\mu_0}\left(1-\widetilde{\mu}_r^{-1}\right)+\frac{B}{\overline{G}}\left(\frac{v^{(1)}M_r^{(1)}}{\mu_r^{(1)}}+\frac{v^{(2)}M_r^{(2)}}{\mu_r^{(2)}}\right), \tag{43}$$

where

$$\widetilde{\mu}_r=\left(\frac{v^{(1)}}{\mu_r^{(1)}}+\frac{v^{(2)}}{\mu_r^{(2)}}\right)^{-1}. \tag{44}$$

Defining the normalized magnetic induction as $B_n=B/\sqrt{\overline{G}\mu_0}$ and normalized remanent magnetization as $M_n^{(\xi)}=M_r^{(\xi)}/\sqrt{\overline{G}/\mu_0}$, Eq. (43) can be written as

$$\lambda^2-\frac{1}{\lambda}=B_n^2\left(1-\widetilde{\mu}_r^{-1}\right)+B_n\left(\frac{v^{(1)}M_n^{(1)}}{\mu_r^{(1)}}+\frac{v^{(2)}M_n^{(2)}}{\mu_r^{(2)}}\right). \tag{45}$$

Note that for the case $M_n^{(\xi)}=0$, expression (45) reduces to the result corresponding to the case for the laminate with soft-magnetic active elastomers (Pathak et al., 2022), namely

$$\lambda^2-\frac{1}{\lambda}=B_n^2\left(1-\widetilde{\mu}_r^{-1}\right). \tag{46}$$

In this case of the soft-magnetic laminate, the application of the external magnetic fields leads to stretching in the $\mathbf{e}_2$ direction.

Fig. 3 shows the dependence of the induced stretch λ on the magnetic induction for various levels of initial magnetization $M_n^{(2)}$; the normalized remanent magnetization of layer 1 is $M_n^{(1)}=-1$. The results are given for HMAE laminates with volume ratio $v^{(1)}=0.5$, and shear modulus contrast $G^{(1)}/G^{(2)}=15$. First, when $M_n^{(2)}$ takes a relatively small positive value (for example, $M_n^{(2)}=+0.2$ in Fig. 3a or $M_n^{(2)}=+0.6$ in Fig. 3b), *compressive* deformation (i.e., $\lambda<1$) developed under a low magnetic induction level (see the red and blue curves in Fig. 3a and b). From a physical point of view, at a low magnetic induction level, the magnetic stress in the HMAE phases is dominated by $-\mathbf{M}_r^{(\xi)}\otimes\mathbf{B}^{(\xi)}/\mu_r^{(\xi)}$, which is positive in layer 1 and negative in layer 2. Since $|M_n^{(1)}|$ is much larger than $|M_n^{(2)}|$, the resulting magnetic stress inside the laminate is positive. At a small magnetic induction level, the resulting positive magnetic stress is larger than the Maxwell stress $\boldsymbol{\sigma}_m^*$ outside the laminate. To satisfy the mechanical traction-free boundary conditions, the magnetic stress inside the laminate is partially compensated by a compressive (negative) mechanical stress, resulting in the compressive deformation. However, as the magnetic induction further increases, the magnetic stress in the HMAE phases is dominated by $\mathbf{B}^{(\xi)}\otimes\mathbf{B}^{(\xi)}/\mu^{(\xi)}$, which is smaller than the Maxwell stress $\boldsymbol{\sigma}_m^*$ outside the laminate, thus, tensile (positive) mechanical stress develops inside the laminate and stretch deformation is observed. Note that, for the case $\mu_r^{(1)}=\mu_r^{(2)}=1.0$ which means the permeability of the HMAE phases equals that of the vacuum surrounding the laminate, only compressive deformation develops (see the black curves in Fig. 3a and b). This is because the magnetic stress inside the laminate is always larger than the Maxwell stress $\boldsymbol{\sigma}_m^*$ outside the laminate due to the positive magnetic stress component $-\mathbf{M}_r^{(1)}\otimes\mathbf{B}^{(1)}/\mu_r^{(1)}$. Second, when the value of $M_n^{(2)}$ is equal to (e.g., $M_n^{(2)}=+1.0$,

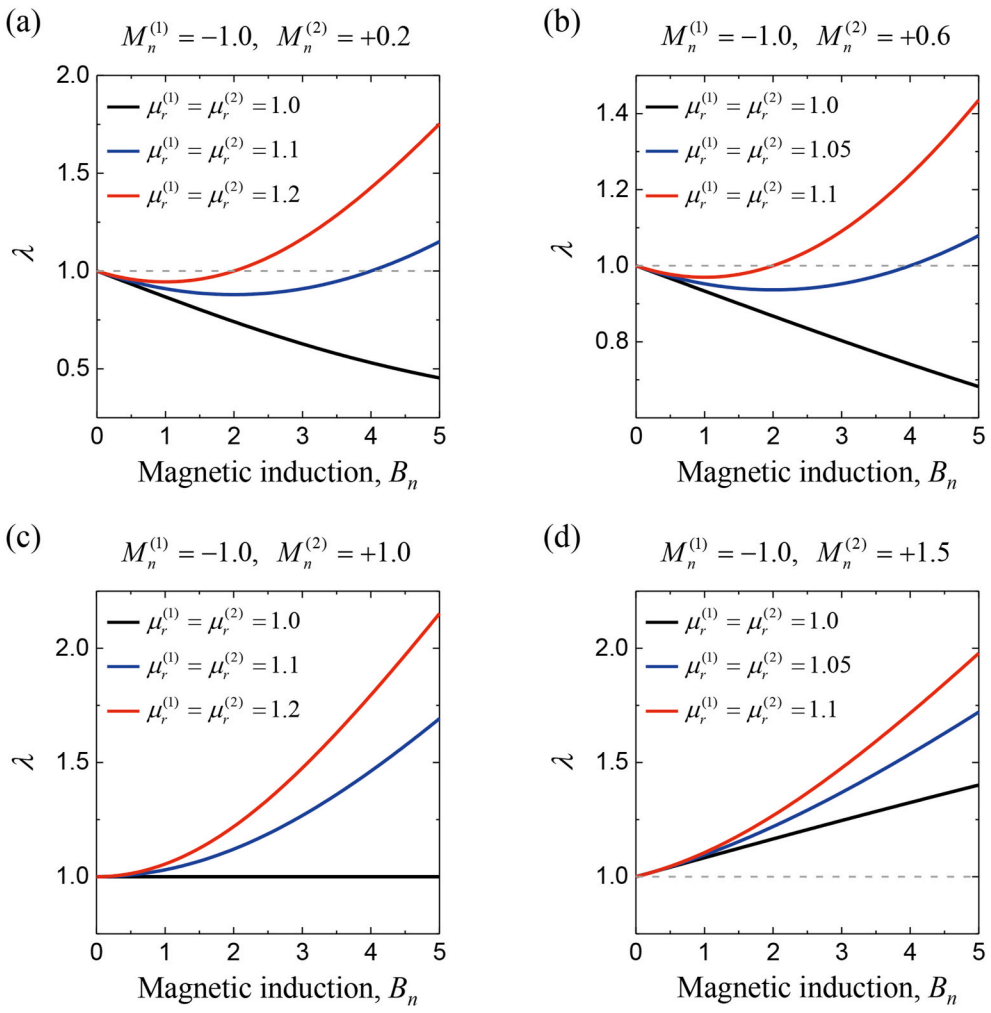

Fig. 3. Magnetic field-induced stretch λ as a function of the normalized magnetic induction $B_n = B/\sqrt{\bar{G}\mu_0}$. The normalized remanent magnetization of layer 1 is fixed at $M_n^{(1)} = -1$, and the normalized remanent magnetization of layer 2 takes the value of (a) $M_n^{(2)} = +0.2$, (b) $M_n^{(2)} = +0.6$, (c) $M_n^{(2)} = +1.0$, and (d) $M_n^{(2)} = +1.5$, correspondingly. The volume ratio and shear modulus contrast are $v^{(1)} = 0.5$ and $G^{(1)}/G^{(2)} = 15$, respectively.

see Fig. 3c) or greater (e.g., $M_n^{(2)} = +1.5$, see Fig. 3d) than the absolute value of $M_n^{(1)}$, only stretch deformation occurs (see the red and blue curves in Fig. 3c and d) because the magnetic stress inside the laminate is smaller than the Maxwell stress $\boldsymbol{\sigma}_m^*$ outside the laminate due to negative magnetic stress component $-\mathbf{M}_r^{(2)} \otimes \mathbf{B}^{(2)}/\mu_r^{(2)}$. In particular, for the case $M_n^{(2)} = +1.0$ and $\mu_r^{(1)} = \mu_r^{(2)} = 1.0$, no deformation occurs in the

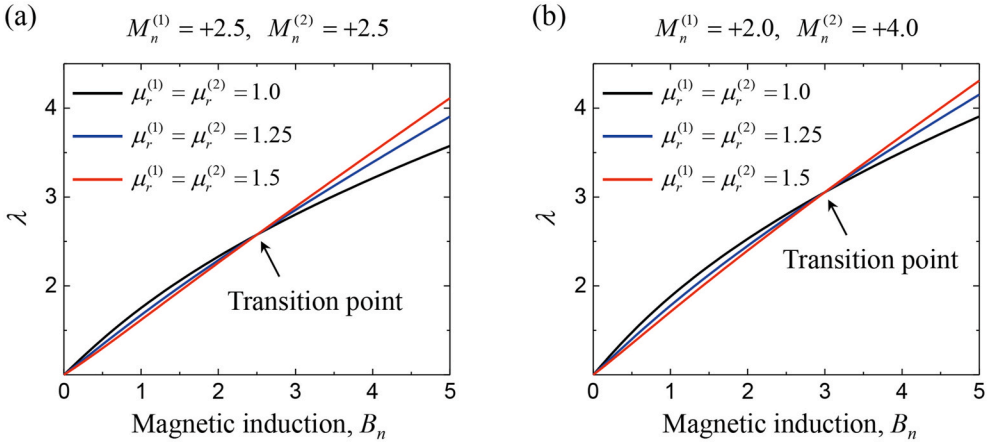

Fig. 4. Magnetic field-induced stretch λ as a function of the normalized magnetic induction $B_n = B/\sqrt{\bar{G}\mu_0}$ for (a) $M_n^{(1)} = M_n^{(2)} = +2.5$ and (b) $M_n^{(1)} = +2.0$, $M_n^{(2)} = +4.0$. The volume ratio and shear modulus contrast are $v^{(1)} = 0.5$ and $G^{(1)}/G^{(2)} = 15$, respectively.

laminate (see the black line in Fig. 3c), since the magnetic stress components $-\mathbf{M}_r^{(1)}\otimes\mathbf{B}^{(1)}/\mu_r^{(1)}$ and $-\mathbf{M}_r^{(2)}\otimes\mathbf{B}^{(2)}/\mu_r^{(2)}$ canceled each other, thus, the magnetic stress inside the laminate equals the Maxwell stress $\boldsymbol{\sigma}_m^*$ outside the laminate.

Fig. 4 shows the dependence of the induced stretch λ on the magnetic induction for laminates in which the remanent magnetizations of both phases are positive (i.e., in the same direction of magnetic induction). The results are given for HMAE laminates with volume ratio $v^{(1)}=0.5$, and shear modulus contrast $G^{(1)}/G^{(2)}=15$. One can see that when the remanent magnetization $M_n^{(\xi)}$ takes relatively large positive values, the stretch λ exhibits a richer evolution phenomenon with the change of relative permeability $\mu_r^{(\xi)}$. Consider the case of $M_n^{(1)}=M_n^{(2)}=+2.5$, as an example: at a relatively small magnetic induction B_n, the stretch λ becomes smaller when the relative permeability $\mu_r^{(\xi)}$ takes a larger value (see Fig. 4a). However, after reaching a transition point at $B_n=2.5$, the stretch λ increases correspondingly as the relative permeability $\mu_r^{(\xi)}$ takes larger values. Similar phenomenon is observed in the laminate with $M_n^{(1)}=+2.0$, $M_n^{(2)}=+4.0$ (see Fig. 4b, the transition point is at $B_n=3.0$). The reason is as follows. When $M_n^{(\xi)}$ is positive, increasing $\mu_r^{(\xi)}$ leads to an increase of the magnetic stress component $-\mathbf{M}_r^{(\xi)}\otimes\mathbf{B}^{(\xi)}/\mu_r^{(\xi)}$ and a decrease of the magnetic stress component $\mathbf{B}^{(\xi)}\otimes\mathbf{B}^{(\xi)}/\mu^{(\xi)}$. At a low magnetic induction level, the component $-\mathbf{M}_r^{(\xi)}\otimes\mathbf{B}^{(\xi)}/\mu_r^{(\xi)}$ dominates the magnetic stress, thus, the magnetic stress inside the laminate increases with an increment in relative permeability $\mu_r^{(\xi)}$. However, the Maxwell stress $\boldsymbol{\sigma}_m^*$ does not change with HAME's magnetic properties, that is, the total stress inside the laminate also remains constant. Therefore, an increase in magnetic stress is compensated by a decrease in mechanical stress. Thus, the laminate undergoes comparatively smaller deformation as the relative permeability $\mu_r^{(\xi)}$ increases. By contrast, for B_n larger than a critical value, the magnetic stress component $\mathbf{B}^{(\xi)}\otimes\mathbf{B}^{(\xi)}/\mu^{(\xi)}$ dominates the magnetic stress, thus, the stretch increases with an increment in relative permeability $\mu_r^{(\xi)}$. Be noted, due to the presence of remanent magnetization in the HMAE laminate, $B_n=0$ does not mean that the external applied magnetic field equals zero. The relation between the magnetic induction inside the laminate and the external applied magnetic field is provided in Appendix A.

3.4. Transverse elastic wave propagation in HMAE laminates

In this section, we consider incremental waves propagating perpendicularly to the layers (i.e., $\mathbf{n}=\mathbf{e}_2$; see Fig. 2c) in the laminate subjected to macroscopically applied magneto-mechanical loads defined in Eq. (29) and Eq. (30). By substituting Eqs. (14), (16), (18), (19), (32) and (35) into (17), we have

$$\frac{\partial^2 u_1^{(\xi)}}{\partial t^2}=\left(c^{(\xi)}\right)^2\frac{\partial^2 u_1^{(\xi)}}{\partial x_2^2},\quad \frac{\partial \dot{p}^{(\xi)}}{\partial x_2}=0,\quad \text{and}\quad \frac{\partial^2 u_3^{(\xi)}}{\partial t^2}=\left(c^{(\xi)}\right)^2\frac{\partial^2 u_3^{(\xi)}}{\partial x_2^2},\tag{47}$$

where

$$c^{(\xi)}=\lambda\sqrt{2\Psi_1^{(\xi)}/\rho^{(\xi)}}.\tag{48}$$

The magnetoelastic moduli tensors for the HMAE phases are given in Appendix B.

Next, substituting Eqs. (15), (16), (18), (19), (32) and (35) into (14) yields

$$\begin{aligned}\dot{\sigma}_{12}^{(\xi)}&=2\lambda^2\Psi_1^{(\xi)}\frac{\partial u_1^{(\xi)}}{\partial x_2}+\frac{B}{\mu^{(\xi)}}\left(B\frac{\partial u_1^{(\xi)}}{\partial x_2}+\dot{B}_1^{(\xi)}\right)\\ \dot{\sigma}_{22}^{(\xi)}&=-\dot{p}^{(\xi)}\\ \dot{\sigma}_{32}^{(\xi)}&=2\lambda^2\Psi_1^{(\xi)}\frac{\partial u_3^{(\xi)}}{\partial x_2}+\frac{B}{\mu^{(\xi)}}\left(B\frac{\partial u_3^{(\xi)}}{\partial x_2}+\dot{B}_3^{(\xi)}\right)\end{aligned}\tag{49}$$

and

$$\begin{aligned}\dot{H}_1^{(\xi)}&=\frac{1}{\mu^{(\xi)}}\left(B\frac{\partial u_1^{(\xi)}}{\partial x_2}+\dot{B}_1^{(\xi)}\right)\\ \dot{H}_3^{(\xi)}&=\frac{1}{\mu^{(\xi)}}\left(B\frac{\partial u_3^{(\xi)}}{\partial x_2}+\dot{B}_3^{(\xi)}\right)\end{aligned}\tag{50}$$

The incremental jump conditions across the interface between alternating layers (at $x_2=0$) corresponding to Eqs. (33) and $(34)_2$ are

$$\begin{aligned}&\dot{\sigma}_{12}^{(1)}=\dot{\sigma}_{12}^{(2)},\quad \dot{\sigma}_{22}^{(1)}=\dot{\sigma}_{22}^{(2)},\quad \dot{\sigma}_{32}^{(1)}=\dot{\sigma}_{32}^{(2)}\\ &\dot{H}_1^{(1)}=\dot{H}_1^{(2)},\quad \dot{H}_3^{(1)}=\dot{H}_3^{(2)}\end{aligned}\tag{51}$$

Substitution of Eqs. (49) and (50) into Eq. (51) yields

$$\Psi_1^{(1)}\frac{\partial u_1^{(1)}}{\partial x_2}\bigg|_{x_2=0}=\Psi_1^{(2)}\frac{\partial u_1^{(2)}}{\partial x_2}\bigg|_{x_2=0},\qquad \Psi_1^{(1)}\frac{\partial u_3^{(1)}}{\partial x_2}\bigg|_{x_2=0}=\Psi_1^{(2)}\frac{\partial u_3^{(2)}}{\partial x_2}\bigg|_{x_2=0}.\tag{52}$$

We seek a solution for Eq. $(47)_1$ in the form

$$u_1^{(\xi)}=A_+^{(\xi)}e^{i\left(k^{(\xi)}x_2-\omega t\right)}+A_-^{(\xi)}e^{i\left(-k^{(\xi)}x_2-\omega t\right)},\tag{53}$$

where ω is the angular frequency, and $k^{(\xi)}=\omega/c^{(\xi)}$ is the wavenumber. The perfect bonding condition between alternating layers enforces

$$u_1^{(1)}\big|_{x_2=0}=u_1^{(2)}\big|_{x_2=0}.\tag{54}$$

Substituting Eq. (53) into Eqs. $(52)_1$ and (54) respectively yields

$$A_+^{(1)}+A_-^{(1)}-A_+^{(2)}-A_-^{(2)}=0\tag{55}$$

and

$$\frac{\Psi_1^{(1)}A_+^{(1)}}{c^{(1)}}-\frac{\Psi_1^{(1)}A_-^{(1)}}{c^{(1)}}-\frac{\Psi_1^{(2)}A_+^{(2)}}{c^{(2)}}+\frac{\Psi_1^{(2)}A_-^{(2)}}{c^{(2)}}=0.\tag{56}$$

Two additional equations for $A_+^{(1)}$, $A_-^{(1)}$, $A_+^{(2)}$, and $A_-^{(2)}$ will be obtained from the Bloch theorem as follows. Rewriting the plane wave solution in Eq. (53) as the Bloch waveform

$$u_1^{(\xi)}=U_1^{(\xi)}(x_2)e^{i(kx_2-\omega t)},\tag{57}$$

where

$$U_1^{(\xi)}(x_2)=A_+^{(\xi)}e^{iK_-^{(\xi)}x_2}+A_-^{(\xi)}e^{-iK_+^{(\xi)}x_2},\tag{58}$$

and $K_\pm^{(\xi)}=k^{(\xi)}\pm k$. According to the Bloch theorem, $U_1^{(\xi)}(x_2)$ must be a periodic function with the period equal to the lattice constant $l=l^{(1)}+l^{(2)}$. Recalling the unit cell shown in Fig. 2c, we have

$$U_1^{(1)}\left(-l^{(1)}\right)=U_1^{(2)}\left(l^{(2)}\right).\tag{59}$$

Substituting Eq. (58) into Eq. (59) yields

$$e^{-iK_-^{(1)}l^{(1)}}A_+^{(1)}+e^{iK_+^{(1)}l^{(1)}}A_-^{(1)}-e^{iK_-^{(2)}l^{(2)}}A_+^{(2)}-e^{-iK_+^{(2)}l^{(2)}}A_-^{(2)}=0.\tag{60}$$

Next, Substituting Eq. (57) and $\dot{B}_1^{(\xi)}=d_1^{(\xi)}(x_2)e^{i(kx_2-\omega t)}$ into Eqs. $(50)_1$ and $(49)_1$ respectively yields

$$\dot{H}_1^{(\xi)} = \mathscr{H}_1^{(\xi)}(x_2)e^{i(kx_2-\omega t)}$$
$$\mathscr{H}_1^{(\xi)}(x_2) = \frac{1}{\mu^{(\xi)}}\left[B\frac{i\omega}{c^{(\xi)}}\left(A_+^{(\xi)}e^{iK_-^{(\xi)}x_2} - A_-^{(\xi)}e^{-iK_+^{(\xi)}x_2}\right) + d_1^{(\xi)}(x_2)\right] \tag{61}$$

and

$$\dot{\sigma}_{12}^{(\xi)} = \mathscr{P}_1^{(\xi)}(x_2)e^{i(kx_2-\omega t)}$$
$$\mathscr{P}_1^{(\xi)}(x_2) = 2\lambda^2\Psi_1^{(\xi)}\frac{i\omega}{c^{(\xi)}}\left(A_+^{(\xi)}e^{iK_-^{(\xi)}x_2} - A_-^{(\xi)}e^{-iK_+^{(\xi)}x_2}\right) + B\mathscr{H}_1^{(\xi)}(x_2) \tag{62}$$

The Bloch theorem implies

$$\begin{aligned}\mathscr{P}_1^{(1)}\left(-l^{(1)}\right) &= \mathscr{P}_1^{(2)}\left(l^{(2)}\right)\\ \mathscr{H}_1^{(1)}\left(-l^{(1)}\right) &= \mathscr{H}_1^{(2)}\left(l^{(2)}\right)\\ d_1^{(1)}\left(-l^{(1)}\right) &= d_1^{(2)}\left(l^{(2)}\right)\end{aligned} \tag{63}$$

Finally, substituting Eq. (62) into Eq. (63) yields

$$\frac{\Psi_1^{(1)}}{c^{(1)}}e^{-iK_-^{(1)}l^{(1)}}A_+^{(1)} - \frac{\Psi_1^{(1)}}{c^{(1)}}e^{iK_+^{(1)}l^{(1)}}A_-^{(1)} - \frac{\Psi_1^{(2)}}{c^{(2)}}e^{iK_-^{(2)}l^{(2)}}A_+^{(2)} + \frac{\Psi_1^{(2)}}{c^{(2)}}e^{-iK_+^{(2)}l^{(2)}}A_-^{(2)} = 0. \tag{64}$$

Combination of Eqs. (55), (56), (60) and (64) yields

$$\det\begin{bmatrix} 1 & 1 & -1 & -1\\ \frac{\Psi_1^{(1)}}{c^{(1)}} & -\frac{\Psi_1^{(1)}}{c^{(1)}} & -\frac{\Psi_1^{(2)}}{c^{(2)}} & \frac{\Psi_1^{(2)}}{c^{(2)}}\\ e^{-iK_-^{(1)}l^{(1)}} & e^{iK_+^{(1)}l^{(1)}} & -e^{iK_-^{(2)}l^{(2)}} & -e^{-iK_+^{(2)}l^{(2)}}\\ \frac{\Psi_1^{(1)}}{c^{(1)}}e^{-iK_-^{(1)}l^{(1)}} & -\frac{\Psi_1^{(1)}}{c^{(1)}}e^{iK_+^{(1)}l^{(1)}} & -\frac{\Psi_1^{(2)}}{c^{(2)}}e^{iK_-^{(2)}l^{(2)}} & \frac{\Psi_1^{(2)}}{c^{(2)}}e^{-iK_+^{(2)}l^{(2)}} \end{bmatrix} = 0 \tag{65}$$

Recalling Eq. (48), Eq. (65) can be reduced to the following dispersion relation $\omega = \omega(k)$,

$$\cos(kl) = \cos\left(\frac{l^{(1)}\omega}{c^{(1)}}\right)\cos\left(\frac{l^{(2)}\omega}{c^{(2)}}\right) - \frac{1}{2}\left(\frac{\rho^{(1)}c^{(1)}}{\rho^{(2)}c^{(2)}} + \frac{\rho^{(2)}c^{(2)}}{\rho^{(1)}c^{(1)}}\right)\sin\left(\frac{l^{(1)}\omega}{c^{(1)}}\right)\sin\left(\frac{l^{(2)}\omega}{c^{(2)}}\right). \tag{66}$$

The layer thicknesses $l^{(\xi)}$ and phase velocity $c^{(\xi)}$ are functions of the stretch ratio as determined by Eq. (28) and Eq. (48), respectively. Note that the obtained dispersion relation for HMAE laminates (66) is identical to that for the purely elastic problem (Galich et al., 2017), and soft-magnetic laminates (Karami Mohammadi et al., 2019). However, the dependence of the stretch on the applied magnetic field differs, resulting in different tunability of the dispersion curves for the different material systems. To illustrate the dependence, one should consider a material model with a stiffening effect (see the discussion of the results for neo-Hookean HMAE laminates in Appendix C). To this end, we consider the HMAE laminate with the phases whose elastic response is dictated by the Gent model, namely

$$\Psi_e^{(\xi)}\left(I_1^{(\xi)}\right) = -\frac{G^{(\xi)}J_m^{(\xi)}}{2}\ln\left(1 - \frac{I_1^{(\xi)} - 3}{J_m^{(\xi)}}\right), \tag{67}$$

where $J_m^{(\xi)}$ is the locking parameter; here, we assume that both phases are characterized by identical locking parameters $J_m^{(1)} = J_m^{(2)} = J_m$. Referring to the steps of Eqs. (37)–(45), the expression for the induced deformation corresponding to the Gent model is

$$\frac{\left(\lambda^2 - \lambda^{-1}\right)J_m}{J_m + 3 - \lambda^2 - 2\lambda^{-1}} = B_n^2\left(1 - \widetilde{\mu}_r^{-1}\right) + B_n\left(\frac{\nu^{(1)}M_n^{(1)}}{\mu_r^{(1)}} + \frac{\nu^{(2)}M_n^{(2)}}{\mu_r^{(2)}}\right). \tag{68}$$

Submitting Eq. (67) into Eq. (48) yields the corresponding phase velocity

$$c_G^{(\xi)} = \lambda\sqrt{\frac{G^{(\xi)}}{\rho^{(\xi)}}\frac{J_m}{J_m + 3 - \lambda^2 - 2\lambda^{-1}}}. \tag{69}$$

By making use of Eqs. (28), (66), (68) and (69), band structure diagrams for transverse waves in the HMAE laminate with alternating Gent phases subjected to the magnetic field perpendicular to the layers are constructed. Fig. 5 illustrates the results for the laminates with $\nu^{(1)} = 0.5$, $\rho^{(1)}/\rho^{(2)} = 1.0$, $G^{(1)}/G^{(2)} = 15$, and $\mu_r^{(1)} = \mu_r^{(2)} = 1.0$; the reported frequency is normalized as $f_n = (\omega L/2\pi)\sqrt{\overline{\rho}/\widetilde{G}}$, where $\overline{\rho} = \nu^{(1)}\rho^{(1)} + \nu^{(2)}\rho^{(2)}$ and $\widetilde{G} = \left(\nu^{(1)}/G^{(1)} + \nu^{(2)}/G^{(2)}\right)^{-1}$. Fig. 5a displays the dispersion curves at $B_n = 0$. In the reported frequency range, four transverse wave band gaps are observed, as highlighted by the shaded areas. The dependence of the transverse wave band gaps on the magnetic induction B_n is shown in Fig. 5b for laminate with phase magnetizations $M_n^{(1)} = -1.0$ and $M_n^{(2)} = -0.5$, and in Fig. 5c for laminate with phase magnetizations $M_n^{(1)} = +1.0$ and $M_n^{(2)} = +0.5$. The magnetic excitation widens and shifts transverse wave band gaps toward higher frequencies. The external magnetic excitation leads to a compression in the laminate with phase magnetizations $M_n^{(1)} = -1.0$ and $M_n^{(2)} = -0.5$, and stretching in the laminate with phase magnetizations $M_n^{(1)} = +1.0$ and $M_n^{(2)} = +0.5$. For instance, at $B_n = 2.5$, the induced deformation corresponding to the phase magnetizations $M_n^{(1)} = -1.0$ and $M_n^{(2)} = -0.5$ is $\lambda = 0.729$, shifting the lower boundary of the first bandgap from $f_n = 0.397$ to 0.593 and widening it from $\triangle f_n = 0.285$ to 0.426. By contrast, the induced deformation in the laminate with the phase magnetizations $M_n^{(1)} = +1.0$ and $M_n^{(2)} = +0.5$ is $\lambda = 1.311$ (at $B_n = 2.5$); the induced deformation

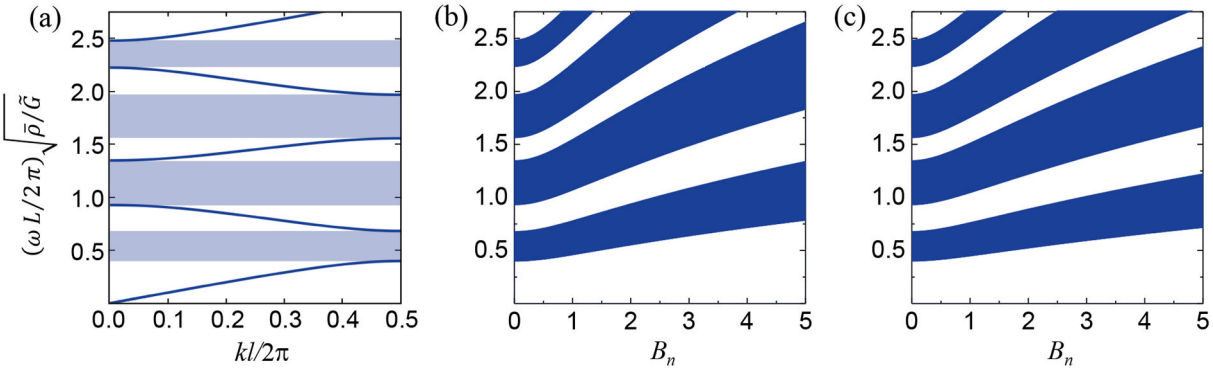

Fig. 5. Tunability of band gap for transverse waves in HMAE laminates with Gent phases; the geometric and material parameters are $\nu^{(1)} = 0.5$, $\rho^{(1)}/\rho^{(2)} = 1.0$, $G^{(1)}/G^{(2)} = 15$, and $\mu_r^{(1)} = \mu_r^{(2)} = 1.0$. (a) The dispersion curves at $B_n = 0$, with the transverse wave band gaps highlighted by the shaded areas. The evolution of the transverse wave band gaps versus B_n for (b) $M_n^{(1)} = -1.0$, $M_n^{(2)} = -0.5$, and (c) $M_n^{(1)} = +1.0$, $M_n^{(2)} = +0.5$. The frequency is normalized as $f_n = (\omega L/2\pi)\sqrt{\overline{\rho}/\widetilde{G}}$.

shifts the lower boundary of the first bandgap from $f_n = 0.397$ to 0.557 and widens it from $\triangle f_n = 0.285$ to 0.399.

4. Conclusion

In this paper, we investigated the behavior of hard-magnetic soft laminates with bi-phasic layered microstructure. We considered the HMAE laminates subjected to a magnetic field perpendicular to the direction of the layers. First, we derived the expression for the magnetic field-induced stretch of the HMAE laminates with remanent magnetizations. The induced stretch is expressed as a function of the volume ratio and the magnetoelastic constants (including the remanent magnetizations) of the HMAE phases. Remarkably, the results indicate that the HMAE laminate undergoes compressive deformation along the direction of the magnetic field when the direction of the remanent magnetizations in the phases is opposite to that of the applied magnetic field. This is in contrast to the previously considered laminates made out of soft-magnetic active elastomers, which can only develop tensile strains in the magnetic field direction.

Second, we examined the propagation of shear waves in the HMAE laminates undergoing finite strains in the presence of an external magnetic field. Interestingly, the derived dispersion relation for HMAE laminates is identical to the one for the purely elastic setting and the one for laminates made of soft-magnetic active elastomers. We note that the bandgap of the shear waves propagating in the direction perpendicular to the layers in the HMAE laminate with neo-Hookean phases is independent of magnetic excitations. However, the dependence of the stretch on the applied magnetic field differs, resulting in different tunability of the dispersion curves for the different material systems. We illustrate this dependence by considering a material model with a stiffening effect; namely, we consider laminates with HMAE Gent phases. We show that the width and position of the shear wave band gaps in the HMAE laminates with remanent magnetizations can be tuned by a remotely applied magnetic field.

The results can guide the design of novel materials with potential applications in remotely controlled wave manipulating devices. We note that the derived exact solutions are based on the material and geometry idealization and may not account for material (Hauseux et al., 2017, 2018; Rappel et al., 2019) or geometrical (Chen et al., 2019; Ding et al., 2021; Yu et al., 2022) uncertainties (or imperfections). These uncertainties in material properties and geometrical (the layer thickness and shape) parameters can affect the wave propagation characteristics in the HMAE laminates. Moreover, the imperfections of the interface or interphase between layers may be introduced in the material manufacturing processes (Arora et al., 2019). The influence of such uncertainties can be quantified through multi-field coupled stochastic analyses (Elouneg et al., 2021; Mazier et al., 2022).

Author agreement

The manuscript has been approved by the authors, **Dr. Quan Zhang** and **Dr. Stephan Rudykh**. This work has not been published previously, and it is not under consideration for publication elsewhere.

Data availability

No data was used for the research described in the article.

Declaration of competing interest

The authors declare that they have no known competing financial interests or personal relationships that could have appeared to influence the work reported in this paper.

Acknowledgment

The authors are grateful for the support of the European Research Council (ERC) through Grant No. 852281- MAGIC.

Appendix A. The relation between the magnetic induction inside the HMAE laminate and external applied magnetic field

Note that we consider an idealization of the periodic microstructure unit cells (shown in Fig. 2) situated far from the specimen boundaries. Under this assumption, the magnetic fields can be considered to be homogeneous in each layer of the laminate and are determined by the jump conditions. According to Eqs. (20) and (30), the magnetic induction B inside the HMAE laminate can be expressed as the applied magnetic field H as follows,

$$B = \left(v^{(1)}\mu^{(1)} + v^{(2)}\mu^{(2)}\right)H + \mu_0\left(v^{(1)}M_r^{(1)} + v^{(2)}M_r^{(2)}\right). \tag{70}$$

Appendix B. The magnetoelastic moduli tensors for the HMAE Phases

We consider HMAE laminates with phases defined by the amended energy function in Eq. (25). By recalling Eq. (36), the tensors of magnetoelastic moduli defined in Eq. (16) are

$$\begin{aligned}
\mathbb{C}_{ijkl}^{(\xi)} &= 2\left(\delta_{ik}b_{lj}^{(\xi)}\Psi_1^{(\xi)} + 2b_{ij}^{(\xi)}b_{kl}^{(\xi)}\Psi_{11}^{(\xi)}\right) + \frac{1}{\mu^{(\xi)}}\delta_{ik}B_l^{(\xi)}B_j^{(\xi)} \\
\mathscr{B}_{ijk}^{(\xi)} &= -\delta_{jk}\frac{1}{\mu_r^{(\xi)}}M_{r|i}^{(\xi)} + \frac{1}{\mu^{(\xi)}}\left(\delta_{ik}B_j^{(\xi)} + \delta_{jk}B_i^{(\xi)}\right) \\
K_{ij}^{(\xi)} &= \frac{1}{\mu^{(\xi)}}F_{ki}^{(\xi)^{-1}}F_{kj}^{(\xi)}
\end{aligned} \tag{71}$$

where $\Psi_1^{(\xi)} = \partial\Psi_e^{(\xi)}/\partial I_1^{(\xi)}$ and $\Psi_{11}^{(\xi)} = \partial\Psi_1^{(\xi)}/\partial I_1^{(\xi)}$; $b_{ij}^{(\xi)}$ is the component of the left Cauchy-Green tensor $\mathbf{b}^{(\xi)} = \mathbf{F}^{(\xi)}\cdot(\mathbf{F}^{(\xi)})^T$, and $M_{r|i}^{(\xi)}$ is the component of the

remanent magnetization $\mathbf{M}_r^{(\xi)}$. According to Eq. (27), we have $M_{r|1}^{(\xi)} = M_{r|3}^{(\xi)} = 0$ and $M_{r|2}^{(\xi)} = M_r^{(\xi)}$.

Appendix C. Band structure for neo-Hookean HMAE laminates

Consider that the purely elastic response of the HMAE phases is described by the neo-Hookean model, submitting Eq. (41) into Eq. (48) yields

$$c_H^{(\xi)} = \lambda\sqrt{G^{(\xi)}/\rho^{(\xi)}}. \tag{72}$$

By making use of Eqs. (28), (45), (66) and (72), the dispersion diagrams for the neo-Hookean HMAE laminate can be constructed. Fig. 6 shows the results for laminates with $\nu^{(1)} = 0.5$, $\rho^{(1)}/\rho^{(2)} = 1.0$, and $G^{(1)}/G^{(2)} = 15$. The dispersion structure is presented in Fig. 6a, with the band gaps highlighted by the shaded areas. The evolution of the first four band gaps with respect to magnetic induction B_n is plotted in Fig. 6b. It can be found that the band gaps are indifferent to the applied magnetic field and induced deformation. The reason can be found by comparing Eq. (28) and Eq. (72), which indicates that the change in the geometry induced by deformation is identical to the change in phase velocity; this implies that the term $l^{(\xi)}/c^{(\xi)}$ in Eq. (66) keeps constant regardless of the value of the magnetic field and the magnetic parameters (including the relative permeabilities and the remanent magnetizations). Therefore, the band gap structures in Fig. 6 are true for any values in relative permeabilities and remanent magnetizations. To achieve magnetic field-induced tunability of the transverse wave band gaps, one should consider laminates with phases exhibiting stronger stiffening (Galich and Rudykh, 2017), for example, Arruda-Boyce or Gent phases.

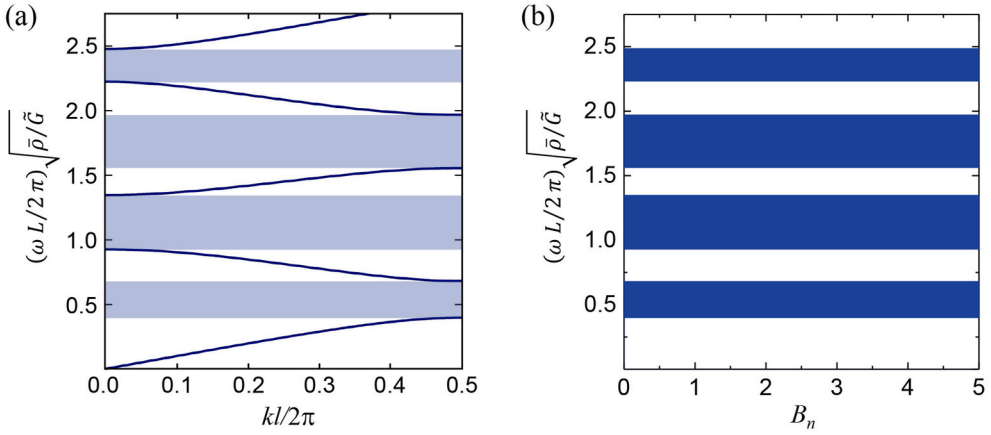

Fig. 6. Dispersion diagrams for transverse waves in HMAE laminates with neo-Hookean phases; the geometric and material parameters are $\nu^{(1)} = 0.5$, $\rho^{(1)}/\rho^{(2)} = 1.0$, and $G^{(1)}/G^{(2)} = 15$. (a) Dispersion curves and (b) the evolution of the first four band gaps with respect to B_n. The frequency is normalized as $f_n = (\omega L/2\pi)\sqrt{\bar{\rho}/\tilde{G}}$.

References

Abd-Alla, A.e.N., Maugin, G.A., 1987. Nonlinear magnetoacoustic equations. J. Acoust. Soc. Am. 82, 1746–1752.

Arora, N., Batan, A., Li, J., Slesarenko, V., Rudykh, S., 2019. On the influence of inhomogeneous interphase layers on instabilities in hyperelastic composites. Materials 12, 763.

Bertoldi, K., Boyce, M.C., 2008. Wave propagation and instabilities in monolithic and periodically structured elastomeric materials undergoing large deformations. Phys. Rev. B 78, 184107.

Bertotti, G., 1998. Hysteresis in Magnetism: for Physicists, Materials Scientists, and Engineers. Gulf Professional Publishing.

Boulanger, P., 1989. Inhomogeneous magnetoelastic plane waves. N.-Holl. Ser. Appl. Math. Mech. 35, 601–606.

Bowen, L., Springsteen, K., Feldstein, H., Frecker, M., Simpson, T.W., von Lockette, P., 2015. Development and validation of a dynamic model of magneto-active elastomer actuation of the origami waterbomb base. J. Mech. Robot. 7, 011010.

Bustamante, R., Dorfmann, A., Ogden, R.W., 2006. Universal relations in isotropic nonlinear magnetoelasticity. Q. J. Mech. Appl. Math. 59, 435–450.

Chen, L.L., Lian, H., Liu, Z., Chen, H.B., Atroshchenko, E., Bordas, S.P.A., 2019. Structural shape optimization of three dimensional acoustic problems with isogeometric boundary element methods. Comput. Methods Appl. Math. 355, 926–951.

Chen, T., Pauly, M., Reis, P.M., 2021. A reprogrammable mechanical metamaterial with stable memory. Nature 589, 386–390.

Crivaro, A., Sheridan, R., Frecker, M., Simpson, T.W., Von Lockette, P., 2016. Bistable compliant mechanism using magneto active elastomer actuation. J. Intell. Mater. Syst. Struct. 27, 2049–2061.

Cui, J., Huang, T.Y., Luo, Z., Testa, P., Gu, H., Chen, X.Z., Nelson, B.J., Heyderman, L.J., 2019. Nanomagnetic encoding of shape-morphing micromachines. Nature 575, 164–168.

Danas, K., Kankanala, S.V., Triantafyllidis, N., 2012. Experiments and modeling of iron-particle-filled magnetorheological elastomers. J. Mech. Phys. Solid. 60, 120–138.

Destrade, M., Ogden, R.W., 2011. On magneto-acoustic waves in finitely deformed elastic solids. Math. Mech. Solid 16, 594–604.

Ding, C., Tamma, K.K., Lian, H., Ding, Y., Dodwell, T.J., Bordas, S.P.A., 2021. Uncertainty quantification of spatially uncorrelated loads with a reduced-order stochastic isogeometric method. Comput. Mech. 67, 1255–1271.

Dorfmann, A., Ogden, R.W., 2003. Magnetoelastic modelling of elastomers. Eur. J. Mech. Solid. 22, 497–507.

Dorfmann, A., Ogden, R.W., 2004. Nonlinear magnetoelastic deformations. Q. J. Mech. Appl. Math. 57, 599–622.

Elouneg, A., Sutula, D., Chambert, J., Lejeune, A., Bordas, S.P.A., Jacquet, E., 2021. An open-source FEniCS-based framework for hyperelastic parameter estimation from noisy full-field data: application to heterogeneous soft tissues. Comput. Struct. 255, 106620.

Erb, R.M., Libanori, R., Rothfuchs, N., Studart, A.R., 2012. Composites reinforced in three dimensions by using low magnetic fields. Science 335, 199–204.

Galich, P.I., Fang, N.X., Boyce, M.C., Rudykh, S., 2017. Elastic wave propagation in finitely deformed layered materials. J. Mech. Phys. Solid. 98, 390–410.

Galich, P.I., Rudykh, S., 2017. Shear wave propagation and band gaps in finitely deformed dielectric elastomer laminates: long wave estimates and exact solution. J. Appl. Mech. 84, 091002.

Galipeau, E., Rudykh, S., deBotton, G., Ponte Castañeda, P., 2014. Magnetoactive elastomers with periodic and random microstructures. Int. J. Solid Struct. 51, 3012–3024.

Garcia-Gonzalez, D., Hossain, M., 2021. Microstructural modelling of hard-magnetic soft materials: dipole–dipole interactions versus Zeeman effect. Extreme Mech. Lett. 48, 101382.

Ginder, J.M., Clark, S.M., Schlotter, W.F., Nichols, M.E., 2002. Magnetostrictive phenomena in magnetorheological elastomers. Int. J. Mod. Phys. B 16, 2412–2418.

Ginder, J.M., Schlotter, W.F., Nichols, M.E., 2001. Magnetorheological elastomers in tunable vibration absorbers. Proc. SPIE 4331 (1), 103–111.

Goshkoderia, A., Chen, V., Li, J., Juhl, A., Buskohl, P., Rudykh, S., 2020. Instability-induced pattern formations in soft magnetoactive composites. Phys. Rev. Lett. 124, 158002.

Goshkoderia, A., Rudykh, S., 2017. Stability of magnetoactive composites with periodic microstructures undergoing finite strains in the presence of a magnetic field. Compos. B Eng. 128, 19–29.

Green, A.E., Rivlin, R.S., Shield, R.T., 1952. General theory of small elastic deformations superposed on finite elastic deformations. Proc. Roy. Soc. Lond. A 211, 128–154.

Guo, D., Chen, Y., Chang, Z., Hu, G., 2017. Longitudinal elastic wave control by pre-deforming semi-linear materials. J. Acoust. Soc. Am. 142, 1229–1235.
Guo, D., Zhang, Q., Hu, G., 2022. Rational design of hyperelastic semi-linear material and its application to elastic wave control. Mech. Mater. 166, 104237.
Haldar, K., Kiefer, B., Menzel, A., 2016. Finite element simulation of rate-dependent magneto-active polymer response. Smart Mater. Struct. 25, 104003.
Hauseux, P., Hale, J.S., Bordas, S.P.A., 2017. Accelerating Monte Carlo estimation with derivatives of high-level finite element models. Comput. Methods Appl. Math. 318, 917–936.
Hauseux, P., Hale, J.S., Cotin, S., Bordas, S.P.A., 2018. Quantifying the uncertainty in a hyperelastic soft tissue model with stochastic parameters. Appl. Math. Model. 62, 86–102.
Hefni, I.A.Z., Ghaleb, A.F., Maugin, G.A., 1995. Surface waves in a nonlinear magnetoelastic conductor of finite electric conductivity. Int. J. Eng. Sci. 33, 2085–2102.
Hu, W., Lum, G.Z., Mastrangeli, M., Sitti, M., 2018. Small-scale soft-bodied robot with multimodal locomotion. Nature 554, 81–85.
Jolly, M.R., Carlson, J.D., Munoz, B.C., 1996. A model of the behaviour of magnetorheological materials. Smart Mater. Struct. 5, 607–614.
Karami Mohammadi, N., Galich, P.I., Krushynska, A.O., Rudykh, S., 2019. Soft magnetoactive laminates: large deformations, transverse elastic waves and band gaps tunability by a magnetic field. J. Appl. Mech. 86, 111001.
Kashima, S., Miyasaka, F., Hirata, K., 2012. Novel soft actuator using magnetorheological elastomer. IEEE Trans. Magn. 48, 1649–1652.
Kim, Y., Yuk, H., Zhao, R., Chester, S.A., Zhao, X., 2018. Printing ferromagnetic domains for untethered fast-transforming soft materials. Nature 558, 274–279.
Kovetz, A., 2000. Electromagnetic Theory. Oxford University Press, Oxford.
Labusch, M., Etier, M., Lupascu, D.C., Schröder, J., Keip, M.-A., 2014. Product properties of a two-phase magneto-electric composite: synthesis and numerical modeling. Comput. Mech. 54, 71–83.
Li, Y., Li, J., Li, W., Du, H., 2014. A state-of-the-art review on magnetorheological elastomer devices. Smart Mater. Struct. 23, 123001.
Lovatt, H.C., Watterson, P.A., 1999. Energy stored in permanent magnets. IEEE Trans. Magn. 35, 505–507.
Lucarini, S., Hossain, M., Garcia-Gonzalez, D., 2022. Recent advances in hard-magnetic soft composites: synthesis, characterisation, computational modelling, and applications. Compos. Struct. 279, 114800.
Lum, G.Z., Ye, Z., Dong, X., Marvi, H., Erin, O., Hu, W., Sitti, M., 2016. Shape-programmable magnetic soft matter. P. Natl. Acad. Sci. USA 113, E6007–E6015.
Makarova, L.A., Alekhina, Y.A., Rusakova, T.S., Perov, N.S., 2016. Tunable properties of magnetoactive elastomers for biomedical applications. Phys. Procedia 82, 38–45.
Maugin, G.A., 1981. Wave motion in magnetizable deformable solids. Int. J. Eng. Sci. 19, 321–388.
Mazier, A., Bilger, A., Forte, A.E., Peterlik, I., Hale, J.S., Bordas, S.P.A., 2022. Inverse deformation analysis: an experimental and numerical assessment using the FEniCS Project. Eng. Comput. 1–15.
Metsch, P., Kalina, K.A., Spieler, C., Kästner, M., 2016. A numerical study on magnetostrictive phenomena in magnetorheological elastomers. Comput. Mater. Sci. 124, 364–374.
Montgomery, S.M., Wu, S., Kuang, X., Armstrong, C.D., Zemelka, C., Ze, Q., Zhang, R., Zhao, R., Qi, H.J., 2020. Magneto-mechanical metamaterials with widely tunable mechanical properties and acoustic bandgaps. Adv. Funct. Mater. 31, 2005319.
Mukherjee, D., Rambausek, M., Danas, K., 2021. An explicit dissipative model for isotropic hard magnetorheological elastomers. J. Mech. Phys. Solid. 151, 104361.
Norris, A.N., Parnell, W.J., 2012. Hyperelastic cloaking theory: transformation elasticity with pre-stressed solids. P. Roy. Soc. A-Math. Phy. 468, 2881–2903.
Ogden, R.W., 2007. Incremental Statics and Dynamics of Pre-stressed Elastic Materials, Waves in Nonlinear Pre-stressed Materials. Springer, Vienna, pp. 1–26.
Opie, S., Yim, W., 2011. Design and control of a real-time variable modulus vibration isolator. J. Intell. Mater. Syst. Struct. 22, 113–125.
Pathak, P., Arora, N., Rudykh, S., 2022. Magnetoelastic instabilities in soft laminates with ferromagnetic hyperelastic phases. Int. J. Mech. Sci. 213, 106862.
Piranda, B., Chodkiewicz, P., Holobut, P., Bordas, S., Bourgeois, J., Lengiewicz, J., 2021. Distributed prediction of unsafe reconfiguration scenarios of modular robotic programmable matter. IEEE T. Robot. 37, 2226–2233.
Ponte Castañeda, P., Galipeau, E., 2011. Homogenization-based constitutive models for magnetorheological elastomers at finite strain. J. Mech. Phys. Solid. 59, 194–215.
Rappel, H., Beex, L.A.A., Hale, J.S., Noels, L., Bordas, S.P.A., 2019. A Tutorial on Bayesian inference to identify material parameters in solid mechanics. Arch. Comput. Methods Eng. 27, 361–385.
Rudykh, S., Bertoldi, K., 2013. Stability of anisotropic magnetorheological elastomers in finite deformations: a micromechanical approach. J. Mech. Phys. Solid. 61, 949–967.
Rudykh, S., Boyce, M.C., 2014. Transforming wave propagation in layered media via instability-induced interfacial wrinklig. Phys. Rev. Lett. 112, 034301.
Saxena, P., Ogden, R.W., 2011. On surface waves in a finitely deformed magnetoelastic half-space. International J. Appl. Mech. 633–665, 03.
Saxena, P., Ogden, R.W., 2012. On Love-type waves in a finitely deformed magnetoelastic layered half-space. Z. Angew. Math. Phys. 63, 1177–1200.
Tang, S.-Y., Zhang, X., Sun, S., Yuan, D., Zhao, Q., Yan, S., Deng, L., Yun, G., Zhang, J., Zhang, S., Li, W., 2018. Versatile microfluidic platforms enabled by novel magnetorheological elastomer microactuators. Adv. Funct. Mater. 28, 1705484.
Tian, T.F., Li, W.H., Deng, Y.M., 2011. Sensing capabilities of graphite based MR elastomers. Smart Mater. Struct. 20, 025022.
Truesdell, C., Toupin, R., 1960. Principles of Classical Mechanics and Field Theory. Springer, pp. 226–858.
Vu, D.K., Steinmann, P., 2007. Nonlinear electro- and magneto-elastostatics: material and spatial settings. Int. J. Solid Struct. 44, 7891–7905.
Wang, L., Zheng, D., Harker, P., Patel, A.B., Guo, C.F., Zhao, X., 2021. Evolutionary design of magnetic soft continuum robots. P. Natl. Acad. Sci. USA 118, e2021922118.
Yan, D., Abbasi, A., Reis, P.M., 2021a. A comprehensive framework for hard-magnetic beams: reduced-order theory, 3D simulations, and experiments. Int. J. Solid Struct. 111319, 00207683.
Yan, D., Pezzulla, M., Cruveiller, L., Abbasi, A., Reis, P.M., 2021b. Magneto-active elastic shells with tunable buckling strength. Nat. Commun. 12, 2831.
Yu, P., Bordas, S.P.A., Kerfriden, P., 2022. Adaptive Isogeometric analysis for transient dynamics: space–time refinement based on hierarchical a-posteriori error estimations. Comput. Methods Appl. Math. 394, 114774.
Zhao, R., Kim, Y., Chester, S.A., Sharma, P., Zhao, X., 2019. Mechanics of hard-magnetic soft materials. J. Mech. Phys. Solid. 124, 244–263.